Nanoscale

PAPER

View Article Online
View Journal | View Issue

Cite this: *Nanoscale*, 2022, **14**, 2502

Hierarchical propagation of structural features in protein nanomaterials†

Ayaka Kamada,‡[a] Anja Herneke,[c] Patricia Lopez-Sanchez,§[c] Constantin Harder,[d,e] Eirini Ornithopoulou,[a] Qiong Wu,[f] Xinfeng Wei,[f] Matthias Schwartzkopf,[d] Peter Müller-Buschbaum,[b,e] Stephan V. Roth,[d,f] Mikael S. Hedenqvist,[f] Maud Langton[c] and Christofer Lendel*[a]

Received 24th August 2021,
Accepted 17th January 2022

DOI: 10.1039/d1nr05571b

rsc.li/nanoscale

Natural high-performance materials have inspired the exploration of novel materials from protein building blocks. The ability of proteins to self-organize into amyloid-like nanofibrils has opened an avenue to new materials by hierarchical assembly processes. As the mechanisms by which proteins form nanofibrils are becoming clear, the challenge now is to understand how the nanofibrils can be designed to form larger structures with defined order. We here report the spontaneous and reproducible formation of ordered microstructure in solution cast films from whey protein nanofibrils. The structural features are directly connected to the nanostructure of the protein fibrils, which is itself determined by the molecular structure of the building blocks. Hence, a hierarchical assembly process ranging over more than six orders of magnitude in size is described. The fibril length distribution is found to be the main determinant of the microstructure and the assembly process originates in restricted capillary flow induced by the solvent evaporation. We demonstrate that the structural features can be switched on and off by controlling the length distribution or the evaporation rate without losing the functional properties of the protein nanofibrils.

Introduction

Nature's own high-performance materials, such as silks and muscles, provide inspiration for the development of new materials with proteins as building blocks. Such materials could play important roles in a range of applications, from sustainable bioplastics and novel foodstuff to sophisticated biomaterials for *e.g.* regenerative medicine. The key to utilize the full potential of the proteins lies in improved knowledge of the hierarchical assembly of the materials, from the molecular level to the macroscopic level.[1] With this in mind, it is notable that proteins show a generic ability of self-assembly into protein nanofibrils (PNF), also referred to as amyloid-like fibrils.[2,3] These species display a highly ordered filamentous structure up to length scales of a few micrometers. The understanding about how protein molecules are transformed into PNFs has increased immensely during the last decades, mainly thanks to the central role of amyloid structures in many devastating diseases.[4,5] Today we have a reasonably good knowledge about how the PNFs are formed from the molecular building blocks, but the ways by which the nanoscale components can be arranged into macroscopic structures remains to a large extent unexplored.[6]

Amyloid-like PNFs are characterized by a highly ordered molecular structure, observable through the cross-β pattern in X-ray fiber diffraction studies,[7] but the PNFs also possess the ability to organize into anisotropic structures at higher length scales. Several studies describe the formation of lyotropic nematic phases in solution.[8–11] Knowles *et al.*[12] demonstrated that films made from PNFs could display nematic order in the presence of plasticizer, in their case polyethylene glycol (PEG). Since then, several studies have explored preparation protocols for PNF-based films[13,14–17] as well as various composite films with PNFs as one constituent.[18–23] However, these studies do

[a]*Department of Chemistry, KTH Royal Institute of Technology, Teknikringen 30, SE-100 44, Stockholm, Sweden. E-mail: lendel@kth.se*
[b]*Heinz Maier-Leibniz Zentrum (MLZ), Technische Universität München, Lichtenbergstraße. 1, D-85748 Garching, Germany*
[c]*Department of Molecular Sciences, SLU, Swedish University of Agricultural Sciences, BioCentrum, Almas allé 5, SE-756 61, Uppsala, Sweden*
[d]*Deutsches Elektronen-Synchrotron, Notkestr. 85, D-22607 Hamburg, Germany*
[e]*Lehrstuhl für Funktionelle Materialien, Physik-Department, Technische Universität München, James-Franck-Str. 1, D-85748 Garching, Germany*
[f]*Department of Fibre and Polymer Technology, KTH Royal Institute of Technology, Teknikringen 56-58, SE-100 44, Stockholm, Sweden*

†Electronic supplementary information (ESI) available. See DOI: 10.1039/d1nr05571b

‡Present address: Department of Chemistry, University of Cambridge, Lensfield Road, Cambridge CB2 1EW, UK.
§Present address: Department of Biology and Biological Engineering, Chalmers University of Technology, SE-412 96, Gothenburg, Sweden.

not address how alterations in fibril nanostructure propagate to larger length scales. Aligned structures in the form of filaments can also be created through flow-assisted assembly processes.[24,25] Another important route to achieve macroscale structures is gel formation. For semi-flexible PNFs with high aspect ratio the critical percolation concentration for sol–gel transition is in the order of 1–2% (w/w).[11] Liquid crystalline structures in solution phase typically occur at lower concentrations than that.[9,11]

A frequently studied PNF system is β-lactoglobulin from bovine whey, either in its pure form or with whey protein isolate (WPI) as starting material.[26] This protein can form PNFs under various conditions, including the use of additives such as alcohols[27] or urea[28] or at low pH.[27,29,30] It has been shown that fibrillation at low pH follows upon hydrolysis of β-lactoglobulin into peptide fragments that constitute the building blocks of the PNFs.[31,32] Furthermore, β-lactoglobulin can form PNFs of distinct morphologies depending on the initial protein concentration.[24,32,33] These classes of fibrils differ in chemical as well as nanomechanical properties and they seem to be constructed from different compositions of molecular building blocks.[32] We have shown that the different classes of fibrils also display distinct behaviors in flow-assisted assembly of protein microfibers with different degree of alignment and substantial differences in mechanical properties of the final fibers.[24] The present study report the discovery of distinct microscale features of solution cast films that appear as a consequence of variation in the nanoscale structures of the β-lactoglobulin PNFs. The process by which the microstructure is formed could reveal new clues about hierarchical material design as they connect the molecular building blocks (below 1 nm) with the microscale features (visible by the human eye). Careful characterization of the PNF films using microscopy and synchrotron X-ray scattering reveal that the ordered structures do not originate from nematic order but rather appear as a consequence of the sol–gel transition and the length distribution of the fibrils. This opens for processing protocols in which the structural and functional properties of the PNFs can be adjusted independently.

Results and discussion

The PNFs used for film preparation were produced from WPI at pH 2 and 90 °C as described previously.[24,32] Different fibril morphologies were obtained by varying the initial protein concentration; all other parameters were the same. Concentrations above 60 mg ml^{-1} resulted in *curved* PNFs (Fig. 1h). These fibrils are short (typically below 500 nm), have a worm-like appearance and a short persistence length (*ca.* 40 nm).[24] Fibril assembly from an initial concentration below 40 mg ml^{-1} resulted in *straight* fibrils that can measure several micrometers in length and have 50 times higher persistence length (*ca.* 1.9 μm) (Fig. 1g).[24] Both classes of fibrils are amyloid-like, as the dimensions agree with the typical numbers for amyloid fibrils, they bind amyloidophilic dyes, such as thioflavin T and Congo red, and display β-sheet rich secondary structure and amyloid-associated intrinsic fluorescence.[32]

Free-standing films were solution cast by letting the PNF dispersions dry on a Teflon surface. Reference films were also prepared from non-fibrillar WPI solution at the same pH. The dry films display the brittleness that is typical for protein films without plasticizer, including PNF-based films.[12] Inspections

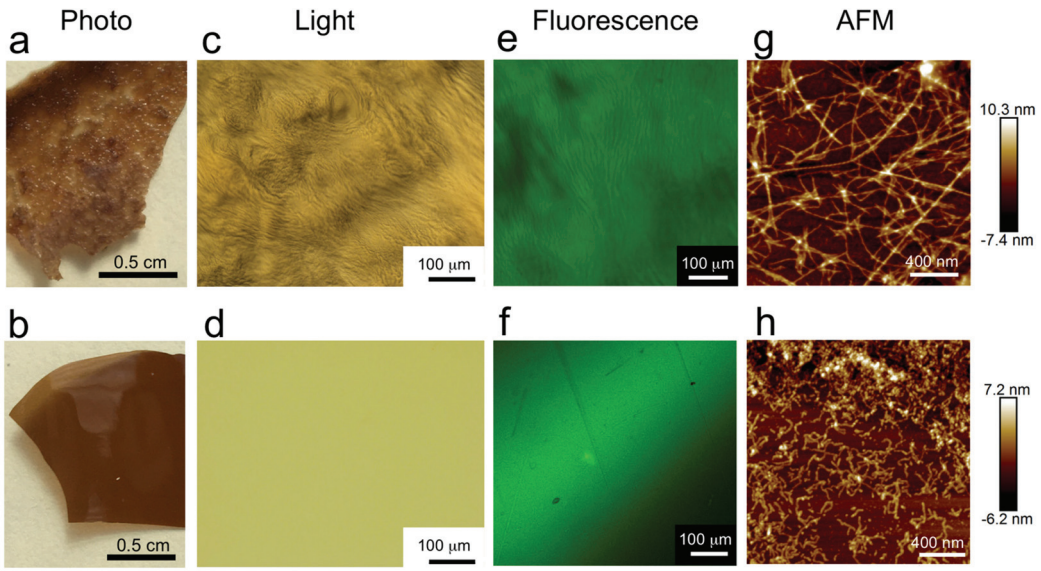

Fig. 1 Films prepared from PNFs with different morphologies result in distinct structural features. Photographs (a and b), light microscopy images (c and d) and confocal laser scanning microscopy images of ThT-stained films (e and f) reveal the presence of domains with apparent aligned structures in films made from *straight* PNFs (top row: a, c, e) while these features are absent in films made from *curved* PNFs (bottom row: b, d, f). AFM images of *straight* (g) and *curved* (h) fibrils show the nanoscale morphology of the two classes of PNFs in diluted samples (1 : 1000).

of the different films by eye and with light microscopy revealed some intriguing differences; while the films made from non-fibrillar WPI or *curved* PNFs were smooth, transparent and apparently homogenous, the films made from *straight* PNFs displayed regions with rough structures interleaved with homogenous regions that are similar to the other films (Fig. 1, Fig. S1†). The rough parts contain apparently ordered domains with resemblance of liquid crystalline polymers.[34] Nematic structures were indeed observed previously in plasticized films by Knowles and co-workers.[12] Our films, however, are made from protein isolate solutions without any additives. The finding is highly reproducible and substrate independent as the same results have been observed for many films made from different batches of PNFs and on different support materials (Teflon, mica, glass, plastics, silicon). We have also observed a similar surface roughness in glycerol-plasticized films cast at pH 7.[23] Film preparations from 2- or 3 times diluted solutions of *curved* fibrils (to match the lower WPI concentration in the *straight* fibril samples) did not change the appearance of the films showing that the observed differences are not an effect of mass concentration. Moreover, purification of the PNFs by dialysis (100 kDa molecular weight cut-off) did not change the structural features. Hence, the structures are a result of the PNFs themselves and not caused in cooperation with non-fibrillar components. Confocal laser scanning microscopy shows evenly distributed thioflavin T (ThT) intensity for both *curved* and *straight* PNFs (Fig. 1e and f), without any indications of spots with extremely high or low local PNF concentration.

The ordered parts appear to consist of aligned structures organized in linear parallel patterns on the micrometer scale (Fig. 1c). These features can also be observed by scanning electron microscopy (SEM) and atomic force microscopy (AFM) (Fig. 2, S2 and S3†). Both these methods show that the dry films are compact without larger cavities. The width of the aligned entities is between 50 and 100 nm, hence they are too wide to be individual PNFs. Some of the SEM images reveal fiber-like structures pointing out from the film (Fig. S2†). However, it is not clear if these 'fibers' are the same as the aligned species as they appear to be wider (>200 nm). To examine if the ordered domains have any orientational order, as expected if they originate from a liquid crystalline phase, we employed polarized optical microscopy but no birefringence could be observed for any of the investigated films (data not shown but similar results are shown in Fig. S4 and S5†).

To further characterize the structure of the ordered domains we performed micro-focused synchrotron X-ray diffraction experiments. The employed beam size was 20 μm × 10 μm, which allows focused measurements within the regions with anisotropic appearance. Wide angle X-rays scattering (WAXS) data of both *straight* and *curved* fibrils clearly display the amyloid associated distances of 4.6 Å and 9.1–9.2 Å (Fig. 3a and b).[7] In addition, there are peaks at 3.7–3.8 Å corresponding to repetitive Cα distances in β-sheets.[35,36] However, neither the WAXS nor the small angle X-ray scattering (SAXS) experiments produced diffraction patterns with anisotropic features (Fig. 3). Hence, the scattering experiments

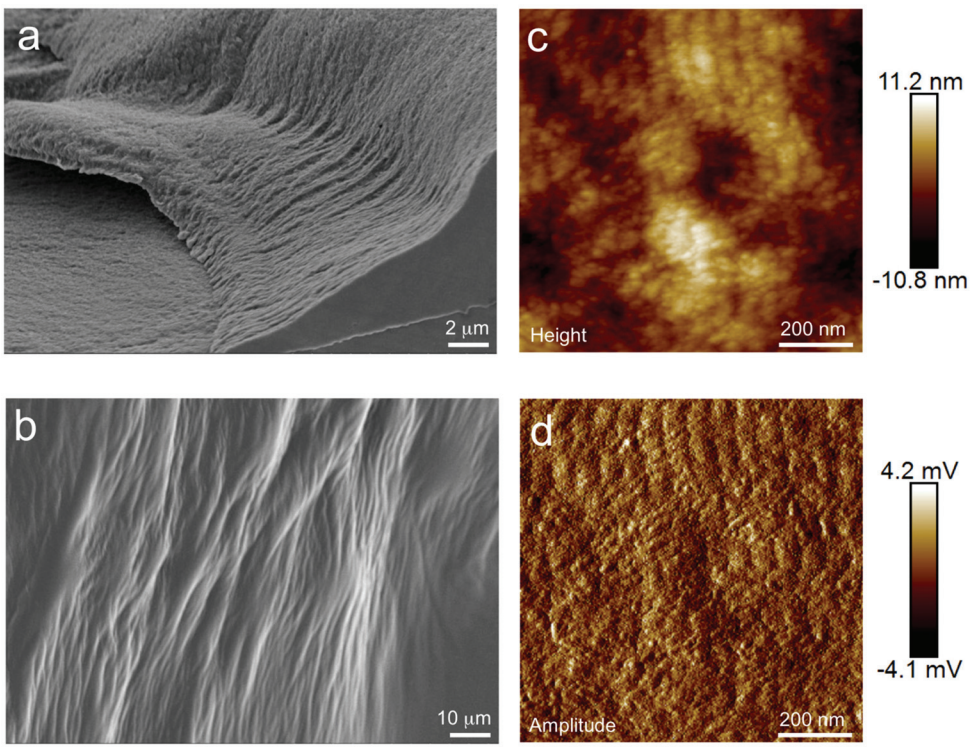

Fig. 2 SEM (a and b) and AFM (c and d) images of the structured domains in films from *straight* PNFs. (a) Fracture surface. (b) Top view of the film surface. (c and d) Height and amplitude AFM images of the same surface area, respectively.

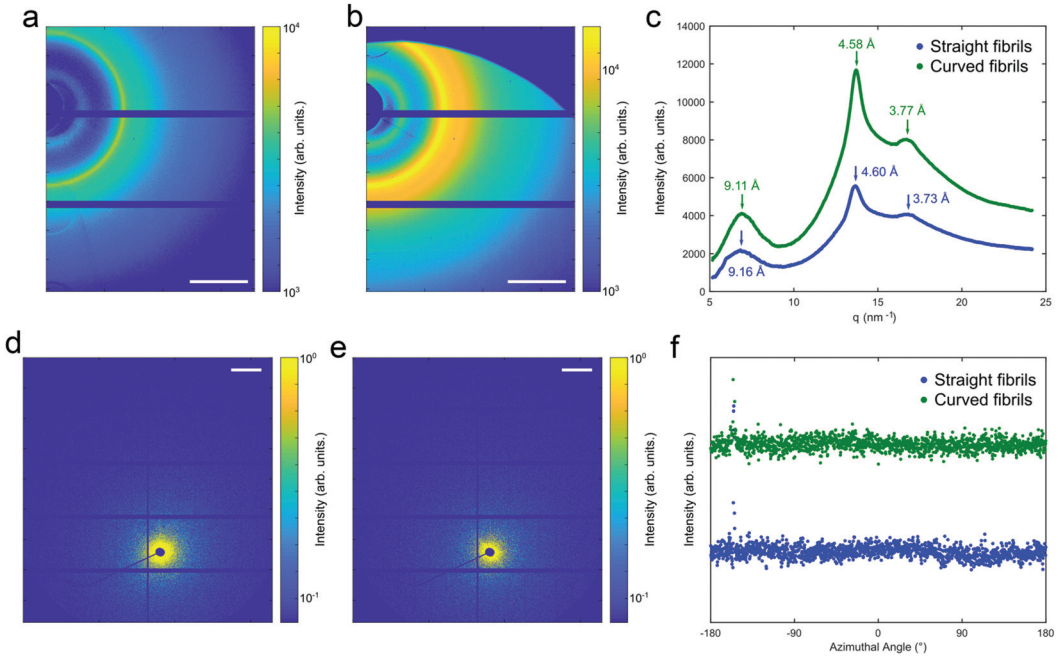

Fig. 3 Synchrotron microfocus X-ray scattering investigation of the PNF films. (a and b) WAXS scattering data for films from *straight* (a) and *curved* (b) PNFs. The scale bars are 10 nm^{-1}. (c) Radial integration of the WAXS data with the corresponding real space distances indicated. (d and e) SAXS scattering data for films from *straight* (d) and *curved* (e) PNFs. The scale bars are 0.2 nm^{-1}. (f) Azimuthal integration of the SAXS data shows isotropic arrangements (in the plane of the film) of the PNFs in both type of films.

confirm the results of the polarized microscopy that there is no overall directional order of the PNFs (in the horizontal plane of the film) for any of the films.

To summarize, the results presented so far show that *straight* PNFs form distinct macroscopic features in solution cast films compared to *curved* fibrils and non-fibrillar protein. Since the starting material and protein constituents are the same in all these films, the structural features must originate from the nanoscale structures. We also found that the structures do not originate from nematic order adopted during drying.

With a closer examination of the PNF dispersions we observed the presence of small (on the order of 100 μm in size) gel domains in the straight PNF samples even though they appeared homogenous from a macroscopic view (Fig. 4, Fig. S4 and S6a†). These domains cover at least 30% of the image area in Fig. S6a.† The occurrence of such domains in the dispersion of the curved fibrils was much less frequent accounting for less than 3% of the image area (Fig. S5 and S6b†). Following the drying process of a 100 μl droplet on a glass surface using light microscopy revealed that the ordered structures appear to form around these gel domains. However, it is not the gel domains themselves that are transformed into the aligned structures; those features instead appear between the domains (Fig. 4, S4, ESI Video S1†). Essentially no birefringence is observed during the drying process, except for some of the gel domains in the starting dispersion (Fig. S4†).

We note that stripe-like patterns with some resemblance of the ordered structures in the PNF films have previously been observed in spray-deposited polymer colloids due to flow and rapid solvent evaporation in confined geometries.[37] Although the time scale for solvent evaporation in the present study is much longer (hours) it appears from the microscopy experiments that the formation of the ordered structures is associated with the drying process (Fig. 4, S4, ESI Video S1†). Drying of a colloidal solution will induce capillary flow in the bulk.[38] This is the origin of the "coffee ring effect" and some accumulation of material in the outer rim can indeed be observed in the films (see Fig. 1, 5 and S8†). However, far from all PNF material is transported to the rim during the drying time. *Straight* PNFs, with persistence lengths of *ca.* 2 μm,[24] behave as rods on micrometer length scale with rotational diffusion times on the order of minutes.[39] As the solvent evaporation proceed, the motions will be slowed down by the inter-fibrillar contacts and the formation of a gel network. A directional capillary flow will speed up the accumulation of PNFs in certain areas, in particular if the available diffusion volume is already reduced close to the pre-formed gel domains. Based on this line of argument, we hypothesized that the appearance of the ordered structures is related to a sol–gel transition that is distorted by capillary flow in a confined space.

The sol–gel transition of the two classes of PNFs depends on their chemical and physical properties. In previous work, we have found that they do display some differences in the chemical properties and probably consist of slightly different peptide segments.[32] To explore if the structural difference of the films could be related to the surface electrostatics of the PNFs their zeta-potential as function of pH was investigated.

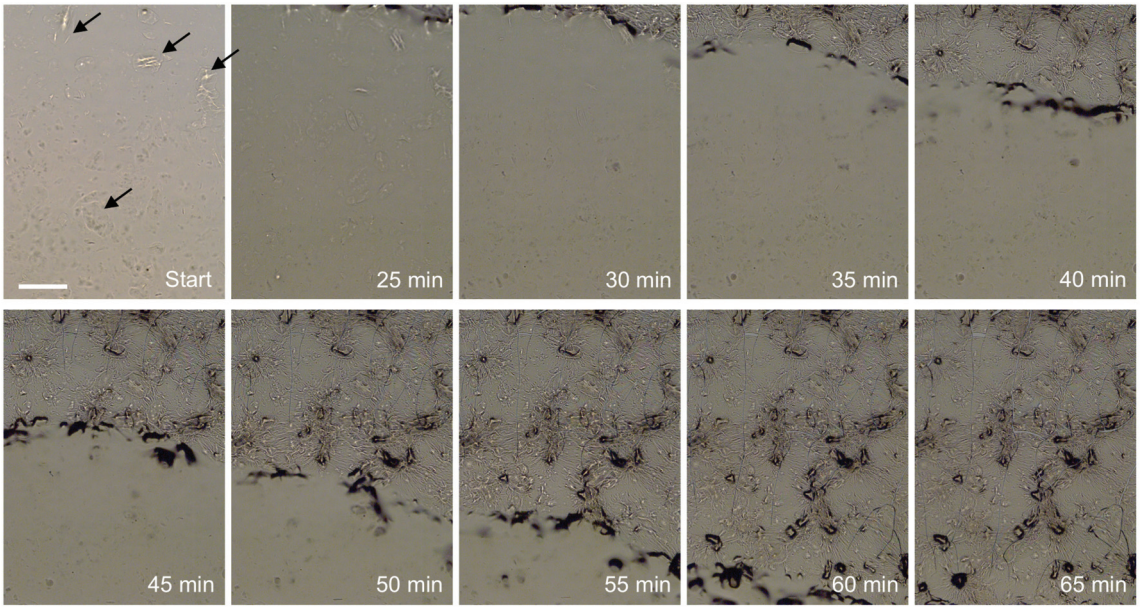

Fig. 4 Film formation (solvent evaporation) followed by light microscopy. 100 μl dispersion of *straight* PNFs were left to dry on a glass surface. Small gel domains (some indicated by the arrows) can be observed already in the start image. The start image with adjusted contrast can be found in Fig. S6A.† Scale bar is 500 μm.

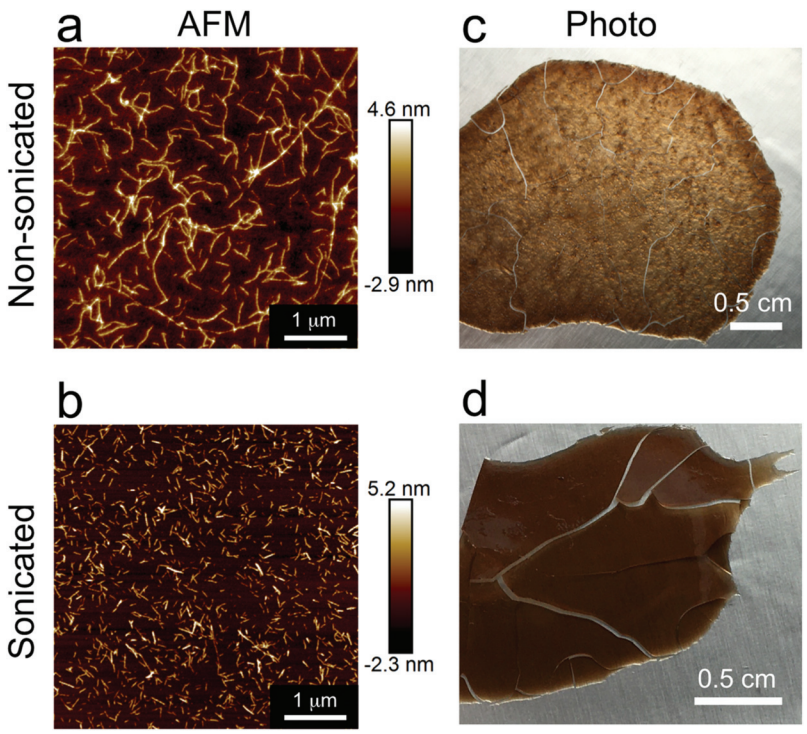

Fig. 5 Comparison of films made from *straight* PNFs without (top row) and with (bottom row) sonication. (a and b) AFM images of diluted PNF solutions. (c and d) Photographs of the dry films.

The results show that the zeta-potentials, as well as the isoelectric points, are similar for the two classes of PNFs and are not likely the reason for the observed structural differences (Fig. S7†). Moreover, preparation of films from solutions with different pH values in the range pH 1 to pH 3 shows the same structural features (Fig. S8†).

Focusing on the physical properties, the *straight* fibrils are characterized by different length distribution and different

stiffness (persistence length, which also incorporates the thickness) compared to the *curved* fibrils. To determine which of these properties (or both) that define the macro-scale structure, we sonicated the straight fibrils (Fig. 5). This resulted in substantially shorter fibrils (but with retained internal structure and stiffness). Typical lengths before sonication was 500–700 nm with some fibrils extending to a few micrometers. After sonication, the majority of the fibrils were shorter than 200 nm. To verify that the amyloid-like structure was retained we compared the ThT fluorescence of sonicated and non-sonicated PNFs. The results show that the fluorescence intensity is in fact higher in the sonicated sample (Fig. S9†). The explanation for this may be that more surface area becomes exposed if aggregated fibrils are also to some degree separated during sonication. We then cast films from non-sonicated and sonicated *straight* PNFs. Interestingly; we found that films made from sonicated fibrils lack the described macroscopic features. Hence, we conclude that the fibril lengths are the source for the observed structures.

Finally, we explored if the appearance of the ordered structures could be omitted by applying a fast evaporation protocol for film formation that would not give the PNFs enough time to accumulate due of capillary flow. Spray deposition allows the application of a very thin layer onto the substrate. We here used a spray device[40] and deposited either straight PNFs or sonicated straight PNFs onto a silicon substrate heated to 55 °C. Deposition was done in 5 or 20 cycles and the films were thereafter investigated by light microscopy.

The microscope images in Fig. 6 and S10† show that the short (sonicated) PNFs form smoother film surfaces than the long (non-sonicated) PNFs. The color variations in the images appear when the thickness of the films corresponds to multiples of half the photon wavelength. Hence, the blue color corresponds to a thickness of *ca.* $n \times 200$ nm, and the magenta color is corresponding to a thickness of *ca.* $n \times 350$ nm, where n is an integer. Already at 5 pulses, larger patches of homogenous thickness (same color) are visible in the film made from short PNFs (Fig. 6b) compared to the long PNFs (Fig. 6a). Fig. S10c† shows the presence of droplets with strong coffee-ring effects confirming that drying occurs at a local scale. At 20 pulses, the color gradients in the film for short PNFs are reduced compared to long PNFs film (Fig. 6a and b) indicating a smoother surface for the sonicated material. However, none of the samples display the ordered microstructures seen in the solution cast films of long *straight* PNFs. Hence, a fast evaporation protocol allows manufacturing of thin films without these structural features, even from long *straight* PNFs.

To conclude, we demonstrated that the macroscale structure of all-protein films is defined by the nanoscale features of the building blocks. Surprisingly, polarized light microscopy and X-ray diffraction show no signs of orientational anisotropy in the apparently ordered domains of the films. Hence, the

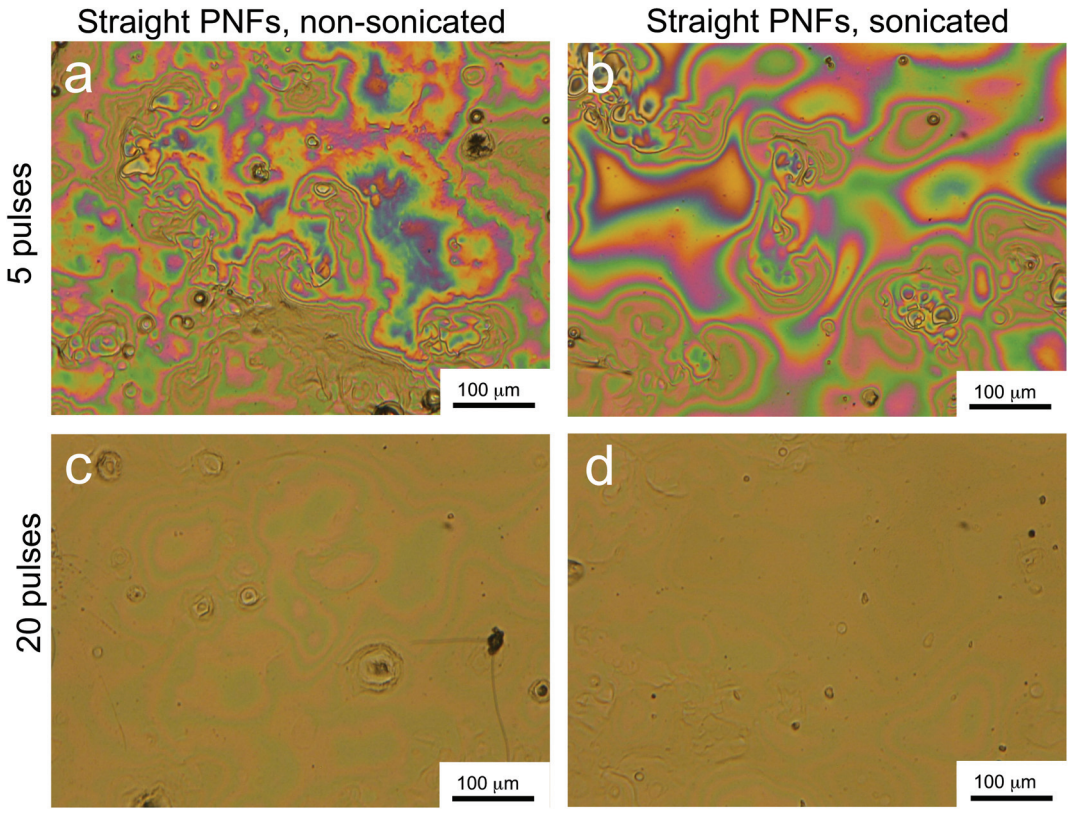

Fig. 6 Light microscopy images of the surface of spray deposited PNF films on silicon. (a and c) *Straight* long PNFs. (b and d) *Straight* short (sonicated) PNFs. (a and b) 5 spray pulses. (c and d) 20 spray pulses.

structural features do not originate from liquid crystalline phases. Rather, the results are in agreement with a mechanism where structural inhomogeneities are created from a local sol–gel transition facilitated by capillary flow during drying in a confined space. Applying a fast-drying protocol suppresses the structural features. The appearance of the macroscale features is directly related to the length distribution of the PNFs and can be switched off by fibril fragmentation. Notably, the amyloid-associated changes in photophysical properties of ThT are retained, or even enhanced, in the fragmented fibrils (Fig. S8†). Hence, controlling the length distribution of the fibrils can be used to define the macroscopic structure of the films without losing the functional properties associated with the surface structure of the PNFs.

Experimental section

Preparation of PNF films

Whey protein isolate (WPI, Lacprodan Di-9224) was kindly provided by Arla Food Ingredients. Solutions for fibrillation reactions were prepared by dissolving WPI in 0.1 M hydrochloric acid (HCl) to a final concentration of *ca.* 100 mg ml^{-1} and then dialyze against 0.01 M HCl (pH 2) using a membrane with 6–8 kDa molecular weight cut-off (Spectrum laboratories). The protein concentrations were then adjusted by addition of dialysis solution. Straight PNFs were obtained from an initial WPI concentration of 40 mg ml^{-1} while curved PNFs were obtained with a starting concentration of 70–80 mg ml^{-1}. Fibrils formed during incubation at 90 °C for a period of 3 days. The yield is typically 20–30% (*i.e.* percentage of the total protein mass incorporated in the PNFs). Purified PNFs were obtained by dialysis for 3 days using a membrane with 100 kDa cut-off (Spectrum laboratories). Films were solution cast by pouring the PNF dispersions onto a poly(tetrafluoroethylene) surface (BYTAC Type AF-21, Saint-Gobain Performance Plastics). Other substrates, including glass, mica, plastics and silicon, were also explored. The films were left to dry in air at room temperature.

Fragmentation of PNFs by sonication

Solutions of straight PNFs were fragmented using a Qsonica Q500 sonicator equipped with a 6 mm micro tip. The amplitude was 20–25% and sonication was done in pulses (2 s on, 10 s off) for a total effective time of 1 or 2 min. During the process the sample was emerged in a water bath.

Film formation by spray deposition

Spray deposition was performed by a spray device (Compact JAU D55000, Spray Systems) onto a piranha-acid cleaned silicon substrate. The PNF suspension (8 mg ml^{-1}) was supplied by a siphon attached to a spray device using the setup described in ref. 40. Spray deposition was carried out by atomization of the PNF suspensions with compressed nitrogen at a gas pressure of 1 bar. The distance between the spray device and the substrate was 200 mm, which means spraying in the very dilute regime. The silicon substrate temperature was controlled to 55 ± 3 °C and the spray protocol consisted of a 0.2 s spraying step followed by 10 s waiting time, repeated for 5 or 20 cycles. This corresponds to deposited average film thickness of $d \approx 0.3$ μm and $d \approx 2$ μm, for the 5 and 20 spray cycles respectively.

Light microscopy

Microscopy investigations were conducted both on pre-formed films dried on a poly(tetrafluoroethylene) surfaces, spray deposited on heated siilcon substrate and *in situ* on samples drying on glass surfaces. From the pre-formed films, a piece of approximately 1 cm × 1 cm was cut and placed onto a glass slide and covered with a glass cover slide. For the *in situ* experiments, 100 μl droplets from dispersions with *straight* or *curved* PNFs were examined while drying into films under ambient conditions. A Nikon Eclipse Ni-U light microscope, with a 10× (0.3 NA) objective was used. Images (polarized and non-polarized) were captured every 5 min with a Nikon Digital Sight DS-Fi2 camera with resolution of 2569 × 1920 pixels. The images were processed with the software NIS-Elements BR (Nikon Instruments Inc.). Microscope images of the sprayed samples were obtained with a Keyence VH Z250R at 500× magnification from the sample center.

Confocal laser scanning microscopy

Films for confocal laser scanning microscopy were prepared by adding 1 mM ThT solution to the PNF samples before drying them into films. The same amount of ThT in relation to total protein content was used in all samples. Fluorescence microscopy was performed using a Zeiss, LSM 780 confocal microscope with ×10 or ×63 objectives. An argon laser was used for excitation at 405 nm and emission was monitored at 450–600 nm.

Scanning electron microscopy (SEM)

Small pieces of the films (*ca.* 1 cm × 1 cm) were sputtered with a platinum/palladium (60/40) alloy using a Cressington 208RH high-resolution sputter and then investigated in a Hitachi S-4800 field-emission SEM.

Atomic force microscopy (AFM)

AFM was carried out using a Dimension FastScan AFM instrument (Bruker). PNF morphology was investigated in tapping mode using samples that were diluted between 1 : 500 and 1 : 10 000 in 10 mM HCl. 25 μl were applied on a freshly cleaved mica surface and dried in air. Film surfaces were examined on non-diluted samples dried on a mica surface. FastScan A cantilevers (Bruker) were used for the experiments and the images were investigated in Nanoscope 1.5 software (Bruker).

Synchrotron X-ray scattering

Wide-angle X-ray scattering (WAXS) and small-angle X-ray scattering (SAXS) were performed at microfocus P03 beamline at PETRA III[41] at DESY, Hamburg, Germany. WAXS intensity was recorded using a Pilatus 300k detector (Dectris, pixel size 172

× 172 mm) with the sample-to-detector distance, SDD = 154 mm. SAXS diffractogram was obtained using Pilatus 1 M detector (Dectris, pixel size 172 × 172 mm) with SDD = 6765 mm. X-ray wavelength of λ = 0.95377 Å was used for both measurements. In order to analyse the structural orientation, the scattering intensity in the range of q = 0.0335–0.4522 nm^{-1} was radically integrated as a function of the azimuthal angle. The data was analysed with DPDAK software.[42]

Dynamic light scattering and zeta potential

Measurements were carried out using a Zetasizer Nano ZS dynamic light scattering instrument (Malvern Instruments). Each sample was measured five times maintaining an attenuation between 7 and 10, and the temperature at 25 °C. The samples were diluted thirty times (30×) before measurements, after first validating that dilution between 10–100× did not significantly affect the value of the zeta potential.

ThT fluorescence

Samples for thioflavin T (ThT) fluorescence measurements were prepared by mixing 0.1 ml PNF solution with 2.4 ml 50 μM ThT solution in PBS buffer. Fluorescence was measured at a Cary Eclipse Spectrofluorometer (Varian) with excitation at 440 nm and emission spectra recorded between 460 and 600 nm.

Author contributions

Ayaka Kamada, Anja Herneke, Patricia Lopez-Sanchez, Constantin Harder, Eirini Ornithopoulou, Qiong Wu, Xinfeng Wei: investigation, writing – review & editing. Matthias Schwartzkopf: investigation, methodology, writing – review & editing. Peter Müller-Buschbaum: supervision. Stephan V. Roth: conceptualization, methodology, writing – review & editing. Mikael S. Hedenqvist: conceptualization, methodology, writing – review & editing. Maud Langton: conceptualization, supervision, writing – review & editing. Christofer Lendel: conceptualization, formal analysis, funding acquisition, investigation, methodology, project administration, supervision, writing – original draft.

Conflicts of interest

There are no conflicts to declare.

Acknowledgements

This work was financially supported by Formas (grant numbers 213-2014-1389 and 2017-00396), Magnus Bergwalls stiftelse (grant number 2015-00858). Parts of this research were carried out at the light source PETRA III at DESY, a member of the Helmholtz Association (HGF).

References

1 T. P. J. Knowles and M. J. Buehler, *Nat. Nanotechnol.*, 2011, **6**, 469–479.
2 T. P. Knowles and R. Mezzenga, *Adv. Mater.*, 2016, **28**, 6546–6561.
3 X. Ye, C. Lendel, M. Langton, R. T. Olsson and M. S. Hedenqvist, in *Industrial Applications of Nanomaterials*, ed. S. Thomas, Y. Grohens and Y. B. Pottathara, Elsevier, 2019, ch. 2, pp. 29–63.
4 P. C. Ke, R. H. Zhou, L. C. Serpell, R. Riek, T. P. J. Knowles, H. A. Lashuel, E. Gazit, I. W. Hamley, T. P. Davis, M. Fändrich, D. E. Otzen, M. R. Chapman, C. M. Dobson, D. S. Eisenberg and R. Mezzenga, *Chem. Soc. Rev.*, 2020, **49**, 5473–5509.
5 F. Chiti and C. M. Dobson, *Annu. Rev. Biochem.*, 2017, **86**, 27–68.
6 C. Lendel and N. Solin, *RSC Adv.*, 2021, **11**, 39188–39215.
7 K. L. Morris and L. C. Serpell, *Methods Mol. Biol.*, 2012, **849**, 121–135.
8 A. M. Corrigan, C. Muller and M. R. H. Krebs, *J. Am. Chem. Soc.*, 2006, **128**, 14740–14741.
9 J. M. Jung and R. Mezzenga, *Langmuir*, 2010, **26**, 504–514.
10 C. Müller and O. Inganäs, *J. Mater. Sci.*, 2011, **46**, 3687–3692.
11 L. M. C. Sagis, C. Veerman and E. van der Linden, *Langmuir*, 2004, **20**, 924–927.
12 T. P. J. Knowles, T. W. Oppenheim, A. K. Buell, D. Y. Chirgadze and M. E. Welland, *Nat. Nanotechnol.*, 2010, **5**, 204–207.
13 L. Wang, F. G. Bäcklund, Y. Yuan, S. Nagamani, P. Hanczyc, L. Sznitko and N. Solin, *ACS Sustainable Chem. Eng.*, 2021, **9**, 9289–9299.
14 A. Kamada, M. Rodriguez-Garcia, F. S. Ruggeri, Y. Shen, A. Levin and T. P. J. Knowles, *Nat. Commun.*, 2021, **12**, 3529.
15 N. M. D. Courchesne, A. Duraj-Thatte, P. K. R. Tay, P. Q. Nguyen and N. S. Joshi, *ACS Biomater. Sci. Eng.*, 2017, **3**, 733–741.
16 F. G. Bäcklund, J. Pallbo and N. Solin, *Biopolymers*, 2016, **105**, 249–259.
17 Y. Yuan and N. Solin, *ACS Appl. Polym. Mater.*, 2021, **3**, 4825–4836.
18 K. J. De France, N. Kummer, Q. Ren, S. Campioni and G. Nyström, *Biomacromolecules*, 2020, **21**, 5139–5147.
19 C. L. Li, J. Adamcik and R. Mezzenga, *Nat. Nanotechnol.*, 2012, **7**, 421–427.
20 L. Wang, B. Xin, A. Elsukova, P. Eklund and N. Solin, *ACS Sustainable Chem. Eng.*, 2020, **8**, 17368–17378.
21 J. Zhao, B. Miao and P. Yang, *ACS Appl. Mater. Interfaces*, 2020, **12**, 35435–35444.
22 S. J. Ling, C. X. Li, J. Adamcik, Z. Z. Shao, X. Chen and R. Mezzenga, *Adv. Mater.*, 2014, **26**, 4569–4574.
23 X. Ye, K. Junel, M. Gällstedt, M. Langton, X. Wei, C. Lendel and M. S. Hedenqvist, *ACS Sustainable Chem. Eng.*, 2018, **6**, 5462–5469.

24 A. Kamada, N. Mittal, L. D. Söderberg, T. Ingverud, W. Ohm, S. V. Roth, F. Lundell and C. Lendel, *Proc. Natl. Acad. Sci. U. S. A.*, 2017, **114**, 1232–1237.
25 A. Kamada, A. Levin, Z. Toprakcioglu, Y. Shen, V. Lutz-Bueno, K. N. Baumann, P. Mohammadi, M. B. Linder, R. Mezzenga and T. P. J. Knowles, *Small*, 2019, **16**, 1904190.
26 S. M. Loveday, S. G. Anema and H. Singh, *Int. Dairy J.*, 2017, **67**, 35–45.
27 W. S. Gosal, A. H. Clark and S. B. Ross-Murphy, *Biomacromolecules*, 2004, **5**, 2408–2419.
28 D. Hamada and C. M. Dobson, *Protein Sci.*, 2002, **11**, 2417–2426.
29 G. M. Kavanagh, A. H. Clark and S. B. Ross-Murphy, *Int. J. Biol. Macromol.*, 2000, **28**, 41–50.
30 C. Veerman, H. Ruis, L. M. C. Sagis and E. van der Linden, *Biomacromolecules*, 2002, **3**, 869–873.
31 C. Akkermans, P. Venema, A. J. van der Goot, H. Gruppen, E. J. Bakx, R. M. Boom and E. van der Linden, *Biomacromolecules*, 2008, **9**, 1474–1479.
32 X. Ye, M. S. Hedenqvist, M. Langton and C. Lendel, *RSC Adv.*, 2018, **13**, 6915–6924.
33 C. C. vandenAkker, M. F. Engel, K. P. Velikov, M. Bonn and G. H. Koenderink, *J. Am. Chem. Soc.*, 2011, **133**, 18030–18033.
34 U. W. Gedde and M. S. Hedenqvist, *Fundamental polymer science*, Springer, 2nd edn, 2019.
35 M. Sunde, L. C. Serpell, M. Bartlam, P. E. Fraser, M. B. Pepys and C. C. Blake, *J. Mol. Biol.*, 1997, **273**, 729–739.
36 L. C. Serpell, *Biochim. Biophys. Acta*, 2000, **1502**, 16–30.
37 A. Buffet, M. M. Abul Kashem, J. Perlich, G. Herzog, M. Schwartzkopf, R. Gehrke and S. V. Roth, *Adv. Eng. Mater.*, 2010, **12**, 1235–1239.
38 R. D. Deegan, O. Bakajin, T. F. Dupont, G. Huber, S. R. Nagel and T. A. Witten, *Nature*, 1997, **389**, 827–829.
39 S. S. Rogers, P. Venema, L. M. C. Sagis, E. van der Linden and A. M. Donald, *Macromolecules*, 2005, **38**, 2948–2958.
40 C. J. Brett, N. Mittal, W. Ohm, M. Gensch, L. P. Kreuzer, V. Korstgens, M. Månsson, H. Frielinghaus, P. Müller-Buschbaum, L. D. Söderberg and S. V. Roth, *Macromolecules*, 2019, **52**, 4721–4728.
41 A. Buffet, A. Rothkirch, R. Döhrmann, V. Körstgens, M. M. A. Kashem, J. Perlich, G. Herzog, M. Schwartzkopf, R. Gehrke, P. Müller-Buschbaum and S. V. Roth, *J. Synchrotron Radiat.*, 2012, **19**, 647–653.
42 G. Benecke, W. Wagermaier, C. H. Li, M. Schwartzkopf, G. Flucke, R. Hoerth, I. Zizak, M. Burghammer, E. Metwalli, P. Müller-Buschbaum, M. Trebbin, S. Forster, O. Paris, S. V. Roth and P. Fratzl, *J. Appl. Crystallogr.*, 2014, **47**, 1797–1803.